The Astrophysical Journal, 933:157 (9pp), 2022 July 10 https://doi.org/10.3847/1538-4357/ac7465

An Expanding Shell of Neutral Hydrogen Associated with SN 1006: Hints for the Single-degenerate Origin and Faint Hadronic Gamma-Rays

H. Sano[1,2], H. Yamaguchi[3,4], M. Aruga[5], Y. Fukui[5], K. Tachihara[5], M. D. Filipović[6], and G. Rowell[7]
[1] Faculty of Engineering, Gifu University, 1-1 Yanagido, Gifu 501-1193, Japan; hsano@gifu-u.ac.jp
[2] National Astronomical Observatory of Japan, Mitaka, Tokyo 181-8588, Japan
[3] Institute of Space and Astronautical Science (ISAS), Japan Aerospace Exploration Agency (JAXA), 3-1-1 Yoshinodai, Chuo-ku, Sagamihara, Kanagawa 252-5210, Japan
[4] Department of Physics, Graduate School of Science, The University of Tokyo, 7-3-1 Hongo, Bunkyo-ku, Tokyo 113-0033, Japan
[5] Department of Physics, Nagoya University, Furo-cho, Chikusa-ku, Nagoya 464-8601, Japan
[6] School of Science, Western Sydney University, Locked Bag 1797, Penrith South DC, NSW 2751, Australia
[7] School of Physical Sciences, The University of Adelaide, North Terrace, Adelaide, SA 5005, Australia
Received 2021 December 27; revised 2022 May 25; accepted 2022 May 26; published 2022 July 12

Abstract

We report new H I observations of the Type Ia supernova remnant (SNR) SN 1006 using the Australia Telescope Compact Array with an angular resolution of $4\farcm5 \times 1\farcm4$ (~2 pc at the assumed SNR distance of 2.2 kpc). We find an expanding gas motion in position–velocity diagrams of H I with an expansion velocity of ~4 km s^{-1} and a mass of ~1000 $M_\odot$. The spatial extent of the expanding shell is roughly the same as that of SN 1006. We here propose a hypothesis that SN 1006 exploded inside the wind-blown bubble formed by accretion winds from the progenitor system consisting of a white dwarf and a companion star, and then the forward shock has already reached the wind wall. This scenario is consistent with the single-degenerate model. We also derived the total energy of cosmic-ray protons W_p to be only ~1.2–2.0 $\times 10^{47}$ erg by adopting the averaged interstellar proton density of ~25 cm^{-3}. The small value is compatible with the relation between the age and W_p of other gamma-ray SNRs with ages below ~6 kyr. The W_p value in SN 1006 will possibly increase up to several 10^{49} erg in the next ~5 kyr via the cosmic-ray diffusion into the H I wind shell.

Unified Astronomy Thesaurus concepts: Supernova remnants (1667); Interstellar medium (847); Cosmic ray sources (328); Gamma-ray sources (633); X-ray sources (1822)

1. Introduction

Identifying the progenitor system of Type Ia supernovae is one of the important issues of modern astrophysics because of their use as standard candles for measuring the expansion history of the universe (e.g., Perlmutter et al. 1999). The single-degenerate (SD) and double-degenerate (DD) models are widely accepted to describe the progenitor systems of Type Ia SNe: the SD model in which a white dwarf accreted gaseous materials from a nondegenerate companion until the white dwarf gets close to the Chandrasekhar mass ~1.4 $M_\odot$ (Whelan & Iben 1973; Nomoto 1982; Iben & Tutukov 1984; Paczynski 1985), and the DD model represents the merger of two white dwarfs (Nomoto 1982; Webbink 1984). To distinguish two scenarios, a search for a surviving companion is thought to be essential because it can be seen only in the SD scenario. Despite many efforts to detect such surviving companions of Type Ia supernova remnants (SNRs), no apparent observational evidence was reported[8] (see reviews by Maoz et al. 2014; Maeda & Terada 2016; Ruiz-Lapuente 2019).

An expanding shell (also known as "wind-blown bubble") of interstellar neutral gas associated with Type Ia SNRs has received much attention as alternative evidence for the SD scenario. Because the expanding gaseous shell could be formed by accretion winds (also known as "disk wind" or "optically thick wind") from the progenitor system consisting of a white dwarf and a nondegenerate companion (e.g., Hachisu et al. 1996, 1999a, 1999b, 2008; Hachisu & Kato 2003a, 2003b), whereas such a wind shell is not expected in the DD scenario. The first discovery of such an expanding gaseous shell was made by CO observations toward Tycho's SNR (Zhou et al. 2016). The authors argued that the expanding shell with the mass of ~220 $M_\odot$ and an expansion velocity of ~5 km s^{-1} could be explained by the energy injection from accretion winds, and hence concluded that Tycho's SNR is consistent with the SD scenario. The presence of a dense-gas wall and the SD scenario were also supported by the rapid shock deceleration during the last ~15 yr (Tanaka et al. 2021). Subsequent CO and H I studies found similar expanding shells of atomic and/or molecular clouds in the Type Ia SNRs: RCW 86 (Sano et al. 2017), N103B (Sano et al. 2018; Alsaberi et al. 2019), and G344.7−0.1 (Fukushima et al. 2020). To better understand the progenitor system of Type Ia supernovae, we need further observations of interstellar molecular and atomic clouds toward other Type Ia SNRs.

SN 1006 (also known as G327.6+14.6) is a historical SNR that exploded in AD 1006 (Stephenson & Green 2002). The small distance of 2.2 kpc from us (Winkler et al. 2003) is consistent with its young age of ~1000 yr and a large diameter of $28\farcm8$ or ~18 pc. Based on the historical record, SN 1006 is widely thought to originate from a Type Ia supernova

[8] Although a strong candidate for a surviving companion was reported in Tycho's SNR named "Tycho G" (González Hernández et al. 2009; Bedin et al. 2014; Xue & Schaefer 2015; Kerzendorf et al. 2018a; Ruiz-Lapuente et al. 2019), the progenitor system for Tycho's SNR is still being debated due to several significant objections (e.g., Kerzendorf et al. 2013; Woods et al. 2017; see also a complete review by Ruiz-Lapuente 2019).

(Schaefer 1996). Owing to its location far from the Galactic plane (∼550 pc), SN 1006 is an ideal object to search for a surviving companion with very little contamination along the line of sight. However, neither a nondegenerated companion nor surviving white dwarf companion has been detected to date (e.g., Schweizer & Middleditch 1980; González Hernández et al. 2012; Kerzendorf et al. 2012, 2018b). Therefore, SN 1006 is thought to be a remnant that exploded as in the DD progenitor system.

SN 1006 is also noted as an ideal site for cosmic-ray acceleration since the first detection of synchrotron X-rays from the northeast and southwest shells (Koyama et al. 1995). Subsequent observations of hard X-rays and GeV/TeV gamma-rays suggest the presence of high-energy cosmic-ray electrons up to ∼100 TeV (e.g., Bamba et al. 2008; Acero et al. 2010; Xing et al. 2016; Condon et al. 2017; Li et al. 2018). Gamma-ray emission is thought to be predominantly the leptonic origin that cosmic-ray electron energies a low-energy photon into the gamma-ray energy via inverse Compton scattering (e.g., Xing et al. 2019).

The interstellar environments of SN 1006, including both the ionized and neutral gaseous medium, have been well studied by multiwavelength observations covering radio to X-rays. Assuming the standard compression ratio for a strong shock of four, the optical, infrared, and X-ray observations estimated the preshock density of ∼0.02–0.4 cm^{-3} from the postshock electron density (e.g., Kirshner et al. 1987; Bamba et al. 2003; Acero et al. 2007; Raymond et al. 2007; Yamaguchi et al. 2008; Katsuda et al. 2009; Miceli et al. 2012; Uchida et al. 2013; Winkler et al. 2013, 2014; Li et al. 2015). For the neutral hydrogen gas surrounding SN 1006, Dubner et al. (2002) carried out H I observations with an angular resolution of $4\farcm7 \times 3\farcm0$ (or 3 pc × 2 pc at the distance of 2.2 kpc). The authors concluded that the H I clouds at V_{LSR}: −25 to −15 $\mathrm{km\,s}^{-1}$ are likely interacting with the SNR, and the derived ambient density is ∼0.3 cm^{-3}. On the other hand, Miceli et al. (2014) argued that the H I clouds at V_{LSR}: ∼6 to 11 $\mathrm{km\,s}^{-1}$ are interacting with the southwest shell of the SNR, by reanalyzing the same H I data sets. They also found that the X-ray shell is slightly deformed in the direction of the southwestern H I cloud. The spatially resolved X-ray spectroscopy along the southwestern shell indicated that the X-ray-derived absorbing column density is proportional to the H I column densities. Moreover, the cutoff energy of the synchrotron emission decreases in the regions corresponding to the southwestern cloud, suggesting that shock–cloud interaction occurred. Therefore, SN 1006 is a suitable site to test the physical relation among the supernova shocks, ambient clouds, and high-energy radiation.

Here, we report the spatial and kinematic distributions of H I clouds toward SN 1006 using new H I observations. Our finding of an expanding H I shell provides a unique solution for the cloud association with SN 1006, as well as its progenitor system and cosmic-ray acceleration. In Section 2 we present the observations and data reductions. Section 3 comprises of four subsections: Section 3.1 gives an overview of X-rays and H I toward SN 1006, Sections 3.2 and 3.3 show the spatial and kinematical distributions of H I while Section 3.4 represents the mass and density of H I. In Sections 4 and 5 we discuss and conclude our findings.

2. Observations and Data Reduction

2.1. H I

We performed H I observations at 1.4 GHz using the Australia Telescope Compact Array (ATCA), which consists of six 22 m antennas located at Narrabri, Australia. Observations were conducted during 24 hr on 2013 November 28, and 2014 March 12, with ATCA in the EW352 and EW367 array configurations (Project ID: C2857). We employed the mosaicking technique, with seven pointings arranged in a hexagonal grid at the Nyquist spatial separation of 19′. The absolute flux density was scaled by observing the quasar PKS 0823−500, which was used as the primary amplitude and bandpass calibrators. We also periodically observed the quasar PKS 1421−490 for gain and phase calibration. We utilized the MIRIAD software package (Sault et al. 1995) for the data reduction. To recover extended emission, we combined the ATCA data cube with archival single-dish data sets obtained using the Parkes 64 m radio telescope (McClure-Griffiths et al. 2009; Kalberla et al. 2010). The resulting beam size of H I is $4\farcm5 \times 1\farcm4$ with a position angle of $11\fdg5$, corresponding to the spatial resolution of 2.9 pc × 0.9 pc at an SNR distance of 2.2 kpc. The typical noise fluctuations are 0.32 K per channel for a velocity resolution of 1 $\mathrm{km\,s}^{-1}$.

2.2. X-Rays

We used archival X-ray data obtained by Chandra with the Advanced Charge Coupled Device (CCD) Imaging Spectrometer I array (Obs IDs: 3838, 4385–4394, 13738–13743, 14423, 14424, and 14435), which have been published by Cassam-Chenaï et al. (2008) and Winkler et al. (2014). We used CIAO version 4.12 (Fruscione et al. 2006) with CALDB 4.9.1 (Graessle et al. 2007) for data reduction and imaging. After reprocessing for all data using the chandra_repro task, we created exposure-corrected, energy-filtered maps using the merge_obs task in the energy bands of 0.5–7.0 keV (broad band), 0.5–1.2 keV (soft band), 1.2–2.0 keV (medium band), and 2.0–7.0 keV (hard band). The resulting effective exposure time is ∼800 ks.

3. Results

3.1. Overview of X-Ray and H I Distributions

Figure 1(a) shows the false-color image of SN 1006 obtained with Chandra. The X-ray morphology of SN 1006 is that of a nearly circular shell in the soft band (red: 0.5–1.2 keV), while the medium-band (green: 1.2–2.0 keV) and hard-band (blue: 2.0–7.0 keV) images show strong bilateral symmetry in the northeast and southwest direction. The soft-band image is dominated by thermal X-rays except for the northeast and southwest shells. The brightest northwestern limb is thought to be formed by interactions between the neutral hydrogen gas and supernova shocks (e.g., Long et al. 2003; Winkler et al. 2014). The hard-band image in the northeast and southwest shells corresponds to nonthermal synchrotron X-rays from cosmic-ray electrons (e.g., Koyama et al. 1995), which is also bright in TeV gamma-rays as shown in contours (Acero et al. 2010).

Figure 1(b) shows the integrated intensity map of H I. In the present paper, we focus on the velocity range from 4.0 to 12.0 $\mathrm{km\,s}^{-1}$, which includes the shock-interacting H I clouds suggested by Miceli et al. (2014). We find H I clouds not only in the west shell, but also toward the north shell and the center of the SNR. Interestingly, no dense H I clouds are adjacent to

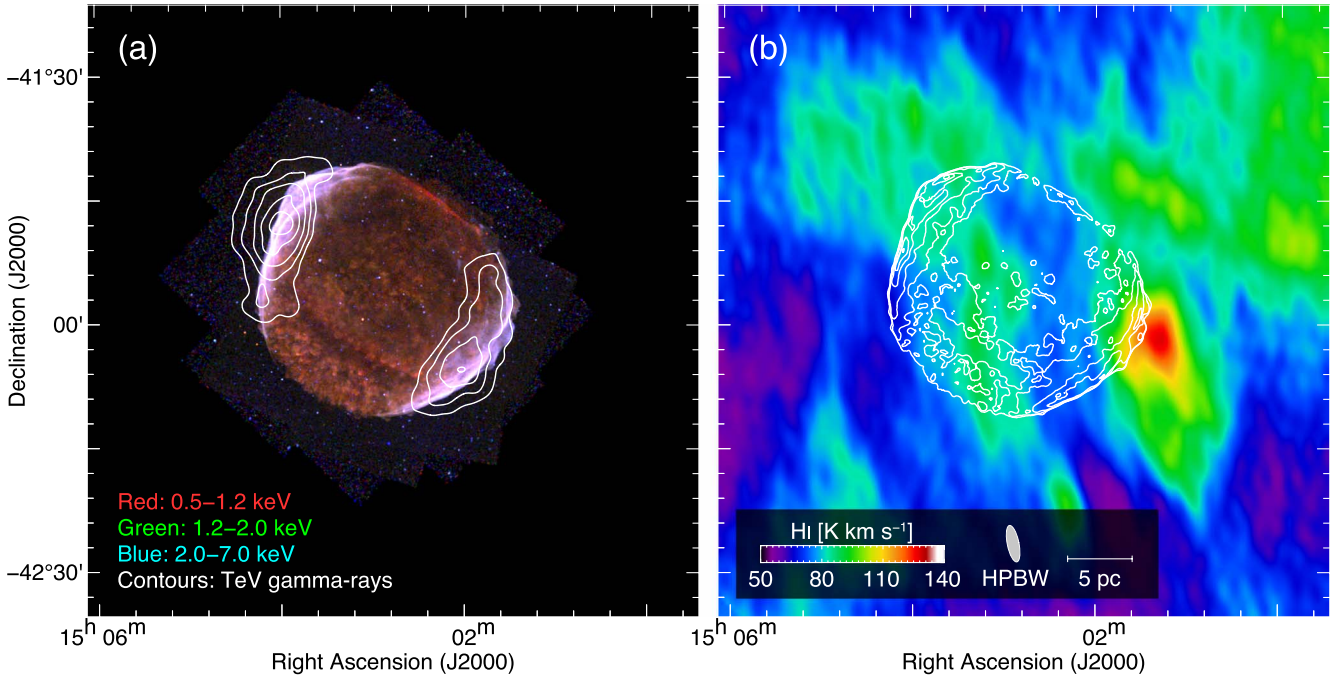

Figure 1. (a) RGB X-ray image of SN 1006 obtained with Chandra (Cassam-Chenaï et al. 2008; Winkler et al. 2014). The red, green, and blue colors correspond to the energy bands 0.5–1.2 keV, 1.2–2.0 keV, and 2.0–7.0 keV, respectively. The superposed contours indicate TeV gamma-ray significance obtained with HESS (Acero et al. 2010). The contour levels are 3, 4, 5, 6, and 7σ. (b) Velocity integrated intensity map of H I obtained with ATCA and Parkes. The integration velocity range is from 4.0 to 12.0 km s^{-1}. The superposed contours indicate the median-filtered Chandra X-ray intensity in the energy band of 0.5–7.0 keV. The contour levels are 2.5, 4.2, 9.3, 17.8, 29.7, and 45.0 $\times$ 10^{-7} photons s^{-1} pixel^{-1}.

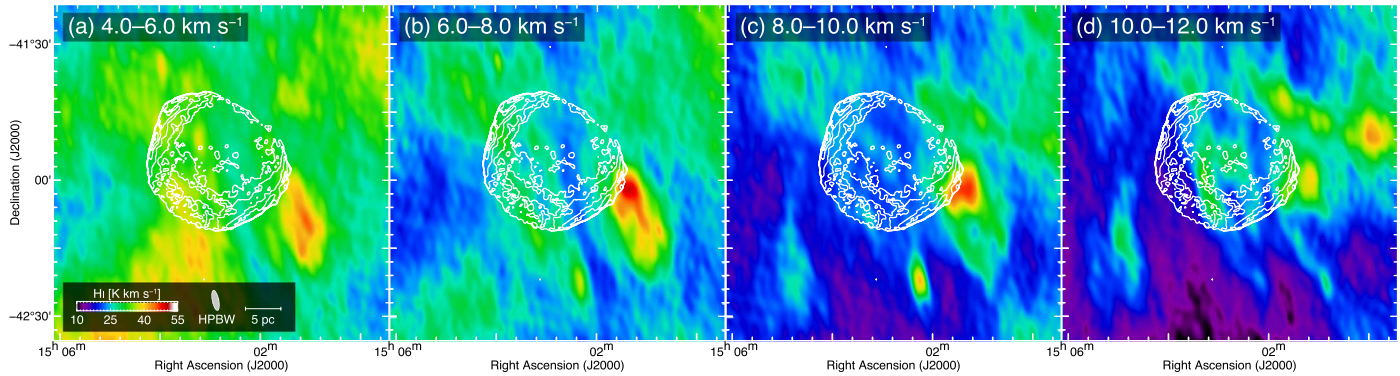

Figure 2. Velocity channel distributions of H I superposed on the Chandra X-ray contours as shown in Figure 1(b). Each panel shows H I intensity map integrated every 2.0 km s^{-1} in a velocity range from 4.0 to 12.0 km s^{-1}.

the southeast shells, where the shock velocity shows the maximum value in SN 1006 (Winkler et al. 2014). We also note that the H I intensity of SN 1006 is about 3–10 times weaker than that of the typical Type Ia SNRs interacting with H I clouds in the Galactic plane (e.g., Sano et al. 2017; Fukushima et al. 2020).

3.2. Velocity Channel Distributions of H I

Figure 2 shows the velocity channel maps of H I toward SN 1006. We find diffuse or clumpy H I clouds, some of which are along with the X-ray shell boundary. The H I clouds at $V_{\rm LSR} = 6.0$–8.0 km s^{-1} lie on the edges of the northeast and southwest X-ray limbs. The northwest shell appears to be associated with H I clumps at $V_{\rm LSR} = 10.0$–12.0 km s^{-1}. The H I intensity at $V_{\rm LSR} = 8.0$–10.0 km s^{-1} decreases toward the center of the SNR, whereas H I clouds fill the remnant in the other velocity maps.

3.3. Spatial and Kinematic Distributions of H I

Figures 3(b) and (d) show the position–velocity (p–v) diagrams in the offset X and Y coordinates, which were rotated by 45 degrees clockwise from the equatorial coordinate as shown in Figure 3(a). Because the H I clouds are distributed across the SNR from northeast to southwest, the rotated image is suitable for extracting the p–v diagram along the H I distribution. We find a cavity-like distribution in each p–v diagram of H I, whose velocity range is from 4.0 to 12.0 km s^{-1}. This trend is not significantly changed by varying the integration spatial ranges of offset X and Y. It is noteworthy that the spatial extent of each H I cavity in the offset X or Y direction is roughly consistent with the apparent diameter of the X-ray shell. We also calculated an average brightness temperature of H I on annuli in about the center of the SNR using the tool KSHELL in the KARMA (Gooch 1996). Figure 3(d) shows the radius–velocity (r–v) diagram centered at

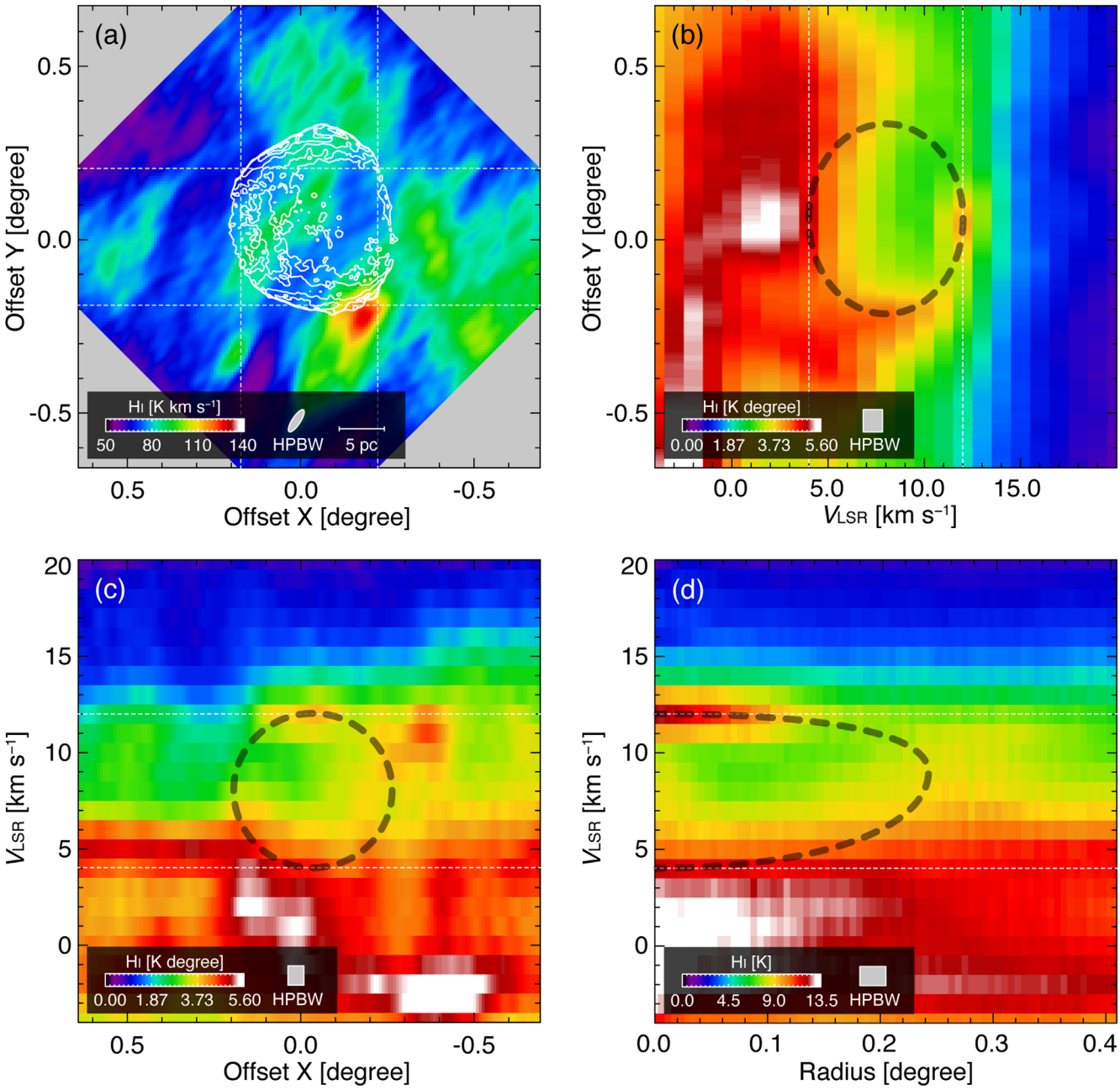

Figure 3. (a) Same image and contours of Figure 1(b), but the map was rotated by 45 degrees clockwise. (b)–(c) Position–velocity (p–v) diagrams of H I. The H I brightness temperature is averaged from $-0.^{\circ}22$ to $0.^{\circ}17$ in offset X for (b) and from $-0.^{\circ}19$ to $0.^{\circ}21$ in offset Y for (c). (d) Radius–velocity (r–v) diagram around the center of the SNR at (α_{J2000}, δ_{J2000}) = ($15^{h}02^{m}51.^{s}1$, $-41^{\circ}55'32.''12$). The black dashed circles in the p–v and r–v diagrams indicate the boundaries of the H I cavities (see the text).

(α_{J2000}, δ_{J2000}) = ($15^{h}02^{m}51.^{s}1$, $-45^{\circ}55'32.''12$).[9] We find a similar cavity-like distribution of H I with the velocity range of V_{LSR}: 4.0–12.0 km s^{-1} and a radius of $0.^{\circ}24$ that is compatible with the shell radius of SN 1006.

3.4. Mass and Density of the H I Clouds

To derive the mass of the H I clouds M_{HI} at V_{LSR}: 4.0–12.0 km s^{-1}, we used the following equation:

$$M_{\rm H\,I} = m_{\rm p}\Omega D^2 \sum_i N_i({\rm H\,I}), \quad (1)$$

where $m_{\rm p}$ is the mass of hydrogen, Ω is the solid angle for each data pixel, D is the distance to the SNR, and N(H I) is the atomic hydrogen column density. In general, N(H I) can be derived as $1.823 \times W$(H I), where W(H I) is the H I integrated intensity. Note that Equation (1) is valid for the optical depth of H I $\ll 1$. However, the latest observational and theoretical studies indicate that almost all H I clouds are optically thick (e.g., Fukui et al. 2014, 2015, 2018; Okamoto et al. 2017; Hayashi et al. 2019; Wang et al. 2020; Seifried et al. 2022). According to Fukui et al. (2015), the optical-depth-corrected H I column density Np′ (H I) is typically twice higher than N (H I) calculated using Equation (1). Since the result was derived using the dust opacity map at 353 GHz (Planck Collaboration

[9] We used the center position of SN 1006, which was derived by Acero et al. (2010).

et al. 2014) toward the intermediate- and high-galactic latitude clouds, this is applicable to SN 1006 at the intermediate latitude of ∼15°. Here, we use a relation presented by Fukui et al. (2015, 2017) that derives $N_{\rm p}'$(H I) as a function of W(H I). We then calculated the mass of the H I clouds within the shell radius of 0.°24 (or ∼9 pc; Acero et al. 2010) is $\sim 1000\,M_{\odot}$ and the averaged atomic hydrogen column density is $\sim 4 \times 10^{20}\,{\rm cm}^{-2}$.

4. Discussion

4.1. Atomic Hydrogen Gas Associated with SN 1006

Miceli et al. (2014) proposed that the southwest H I cloud, peaked at $\sim 8\,{\rm km\,s}^{-1}$, is interacting with the SNR, by comparing spatial distributions of the H I cloud, the indentation of the X-ray shell, and the cutoff energy of synchrotron emission. Here, we suggest that the H I clouds at $V_{\rm LSR} = 4.0$–$12.0\,{\rm km\,s}^{-1}$ are most likely associated with the SNR from a kinematic point of view.

We first argue that the cavity-like distributions of H I in the p–v and r–v diagrams provide us with a hint for the physical association with the atomic hydrogen gas at the velocity range of 4.0–12.0 km s^{-1}. Because such cavity-like distributions in an SNR represent an expanding gas, they are thought to be formed by shock waves and/or strong winds from the progenitor system of the SNR (e.g., Koo et al. 1990; Koo & Heiles 1991; Hachisu et al. 1999a, 1999b). In the case of SN 1006, the expansion velocity is $\sim 4\,{\rm km\,s}^{-1}$ centered at the systemic velocity of $8 \pm 2\,{\rm km\,s}^{-1}$. It is also noteworthy that the projected wind shell gives the maximum extent near the systemic velocity, where we find a hollowed-out distribution of H I as shown in Figure 2(c). Moreover, the maximum spatial extent of the expanding shell is found to be roughly the same size of the SNR shell as shown in Figure 3. This indicates that the forward shock has already reached the wind shell, because the free expansion phase inside the shell is short enough owing to a much lower density (e.g., Weaver et al. 1977). In fact, Badenes et al. (2007) have already predicted such a situation using the one-dimensional numerical simulation. This can naturally explain the indentation of the X-ray shell toward the southwest H I cloud suggested by Miceli et al. (2014).

Next, we emphasize that the H I-derived systemic velocity at $\sim 8\,{\rm km\,s}^{-1}$ coexists with the conventional source distance of 2.2 kpc. Although the systemic velocity at the distance of 2.2 kpc represents about $-32\,{\rm km\,s}^{-1}$ by adopting the Galactic rotation curve model (Brand & Blitz 1993) with conventional Galactic parameters of $R_0 = 8.5$ kpc and $\Theta_0 = 220\,{\rm km\,s}^{-1}$ (IAU recommended values; Kerr & Lynden-Bell 1986), the velocity difference about $40\,{\rm km\,s}^{-1}$ is not a problem since SN 1006 is placed almost 600 pc away from the Galactic plane. This implies that SN 1006 and its surrounding gas do not follow the Galactic rotation as also pointed out by Dubner et al. (2002) and Miceli et al. (2014).

The almost circular shape of SN 1006 without strong deformation is naturally expected by considering the column density of the shocked clouds (e.g., Lopez et al. 2009; Bozzetto et al. 2017). In general, the shell morphology approaches a circular shape with decreasing the density of shock-associated clouds (e.g., Filipović et al. 2022). The young TeV gamma-ray SNR RX J0852.0−4622 (∼1700 yr) is a good example because the SNR shows an almost circular shell. The total interstellar proton column density of shock-associated clouds is $\sim 3 \times 10^{21}\,{\rm cm}^{-2}$ for RX J0852.0−4622 (Fukui et al. 2017; Maxted et al. 2018). By contrast, young (∼1600 yr) TeV gamma-ray SNR RX J1713.7−3946 shows a strongly deformed X-ray shell owing to shock-interactions with dense clouds of $\sim 7 \times 10^{21}\,{\rm cm}^{-2}$ as averaged column density (e.g., Fukui et al. 2003, 2012, 2021; Sano et al. 2010, 2013, 2015). In the case of SN 1006, the column density of the shocked H I cloud is $\sim 4 \times 10^{20}\,{\rm cm}^{-2}$ (see Section 3.4). Because the cloud density in SN 1006 is at least one order of magnitude smaller than that in the three similar SNRs, the almost circular shape of SN 1006 is expected even if the shock–cloud interactions occurred.

Moreover, the previous proper-motion measurements may also be consistent with the H I distributions at $V_{\rm LSR} = 4.0$–$12.0\,{\rm km\,s}^{-1}$. According to Winkler et al. (2014), the highest velocity of $\sim 7400 \pm 800\,{\rm km\,s}^{-1}$ was found in the southeast shell where no dense H I clouds are located (see Figure 1(b)). On the other hand, the slower shock velocities of $\sim 5000\,{\rm km\,s}^{-1}$ are seen in the northeast and southwest shells with rich H I clouds (see also Figure 1(b)). By considering the forward shock interaction with the inner wall of the H I shell, we can possibly find rapid deceleration of the shock wave toward the northeast and southwest shells of SN 1006 (e.g., Tanaka et al. 2021).

In conclusion, we claim that the H I clouds at $V_{\rm LSR} = 4.0$–$12.0\,{\rm km\,s}^{-1}$ are likely associated with SN 1006 in terms of their spatial distributions, kinetics, and physical properties.

4.2. A Hint for a Single-degenerate Origin

As described in Section 3.4, the expanding H I shell associated with SN 1006 has a mass of $\sim 1000\,M_{\odot}$. If the ambient medium with this large mass was uniformly distributed over the present volume of the remnant before being blown out, the initial ambient density is estimated to be $\sim 12\,{\rm cm}^{-3}$ (here we assumed the shell radius of ∼9 pc; Acero et al. 2010). On the other hand, previous X-ray studies indicated the low preshock density of ~ 0.02–$0.4\,{\rm cm}^{-3}$, based on the high velocity of the SNR forward shock (e.g., Katsuda et al. 2009; Winkler et al. 2014) and low ionization state of the postshock interstellar medium (ISM) and Fe ejecta (Acero et al. 2007; Yamaguchi et al. 2014). This discrepancy implies that the expanding H I shell was first formed by the strong preexplosion winds and subsequently the progenitor of SN 1006 exploded inside the low-density cavity.

Because such wind activity prior to a Type Ia supernova explosion is thought to be associated with the SD scenario, we discuss whether the typical SD progenitor system can form the expanding H I shell discovered in SN 1006. Hachisu et al. (1999a, 1999b) presented that the typical wind mass-loss rate is $\sim 2 \times 10^{-6}\,M_{\odot}\,{\rm yr}^{-1}$ (up to $\sim 10^{-4}\,M_{\odot}\,{\rm yr}^{-1}$; see also Nomoto et al. 2005) and the wind velocity is $\sim 2000\,{\rm km\,s}^{-1}$. If we adopt the dynamical timescale of an expanding H I shell as the wind duration period, we derive the momentum of accretion winds to be $\sim 8000\,M_{\odot}\,{\rm km\,s}^{-1}$ or more. On the other hand, the momentum of an expanding H I shell is to be $\sim 4000\,M_{\odot}\,{\rm km\,s}^{-1}$, by adopting the expansion velocity of $\sim 4\,{\rm km\,s}^{-1}$ and the H I cloud mass of $\sim 1000\,M_{\odot}$. Therefore, the SD scenario can adequately explain the momentum of the observed expanding H I shell.

Finally, we discuss whether only the SD channel can produce the optically thick winds through a phase of accreting material from a companion. According to Ivanova et al. (2013), the DD channel also undergoes several phases in their evolution that are not clear, in particular, the "common envelope phase." The DD

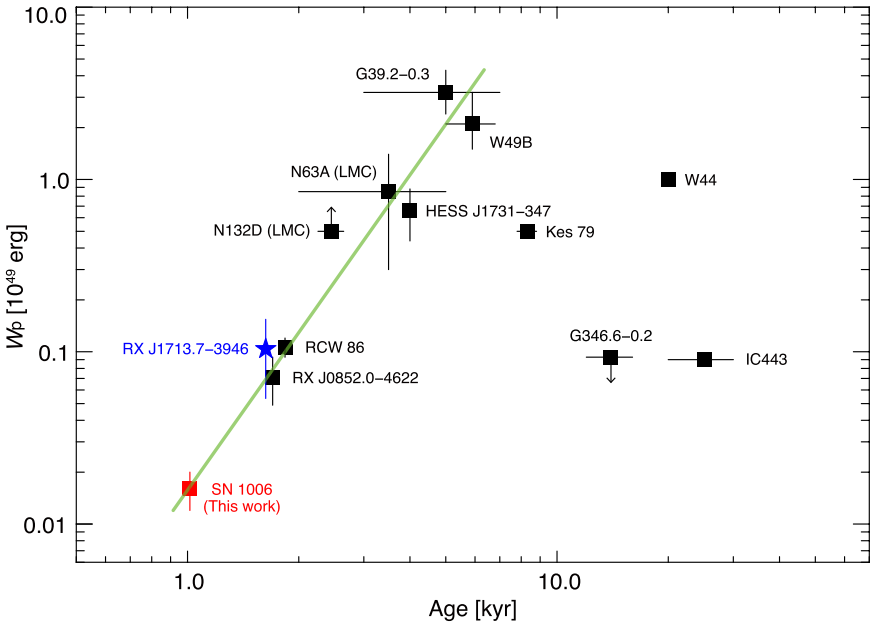

Figure 4. Scatter plot between the age of SNRs and the total energy of cosmic-ray protons W_p (Sano et al. 2021b). The green line indicates the linear regression of the double-logarithmic plot applying the least-squares fitting for data points with the ages of SNRs below 6 kyr. The hadronic gamma-ray luminosity for each SNR was derived from the previous SED modeling alone except for RX J1713.7−3946 (see the text).

channel also experiences stages of accretion but may be not stable enough or extended sufficiently in time compared to the SD channel. Since there are phases that we do not understand well in the DD channel, this uncertainty is a limitation of the present study to distinguish the SD and DD models. Another possibility is that a red supergiant with strong stellar winds happened to be in the line of sight. This possibility has been eliminated by the previous dedicated studies of a companion star search (e.g., Schweizer & Middleditch 1980; González Hernández et al. 2012; Kerzendorf et al. 2012, 2018b). In any case, we would emphasize that the present H I results and current knowledge also favor the SD scenario as the explosion mechanism of SN 1006, nevertheless, no surviving companion has been detected.

4.3. Total Energy of Cosmic-Ray Protons

SNRs are thought to be promising acceleration sites for cosmic-ray protons, up to at least a few Peta electronvolts through the diffusive shock acceleration (DSA; e.g., Bell 1978; Blandford & Ostriker 1978). By considering the injection rate of cosmic rays and the total power of supernova explosions, the conventional value of the total energy of cosmic-ray W_p is to be $\sim 10^{49}$–10^{50} erg per supernova explosion. Since W_p is proportional to the gamma-ray luminosity and the inverse of gas density, we can constrain the value of W_p for each SNR by observations. However, observational values of W_p still had large ambiguities because of the lack of unified quantification for shock-interacting molecular/atomic clouds through the CO/H I radio line observations.

Most recently, Sano et al. (2021a, 2021b) summarized observational W_p values for 12 gamma-ray SNRs by adopting the number densities of shocked clouds using CO/H I data sets. The authors found a tight relation between the SNR age and W_p for 12 gamma-ray SNRs: The young SNRs below ∼6 kyr show a positive correlation between them, while the older SNRs more than ∼8 kyr show a steady decrease of W_p. The authors proposed that this trend can be explained as a combination of the age-limited acceleration (e.g., Ohira et al. 2010) and the energy-dependent diffusion of cosmic rays (e.g., Aharonian & Atoyan 1996; Gabici 2013). If the trend is real, SN 1006 shows a much lower value of W_p because of the low gamma-ray luminosity and gas density as well as its young age. In the present section, we derive the W_p value of SN 1006 and compare it with other gamma-ray SNRs.

According to the latest broadband spectral modeling of SN 1006, gamma-ray emission is leptonic-dominated, which was produced from the inverse Compton scattering between accelerated cosmic-ray electrons and interstellar photons. On the other hand, hadronic gamma-rays, produced by interactions between cosmic-ray protons and interstellar protons, are thought to be partially contributed. The total energy of accelerated cosmic-ray protons W_p is derived by Xing et al. (2019) as:

$$W_p = 1.5 - 2.5 \times 10^{49} (n/0.2\ \mathrm{cm}^{-3})^{-1}\ \mathrm{erg}, \quad (2)$$

where n is the number density of interstellar protons. In SN 1006, the averaged interstellar proton density is estimated to be $\sim 25\ \mathrm{cm}^{-3}$ by adopting a shell radius of 0°.24 or ∼9.2 pc and a shell thickness of 0°.05 or ∼1.9 pc (Acero et al. 2010). We then obtained $W_p = 1.2$–2.0×10^{47} erg, which corresponds to ∼0.02% of the typical released kinetic energy of a supernova explosion of $\sim 10^{51}$ erg.

Figure 4 shows the scatter plot between the SNR age and W_p for 13 gamma-ray SNRs that are listed in Table 1. Note that the hadronic gamma-ray luminosity for deriving the W_p value in each SNR was calculated by the spectral energy distribution (SED) modeling alone except for RX J1713.7−3946 (see also Fukui et al. 2021). We find that SN 1006 lies on the regression line, which was fitted using the data points with the ages of SNRs below 6 kyr, suggesting that the positive relation between the SNR age and W_p is applicable to gamma-ray SNRs with ages at least ∼1–6 kyr. If so, the W_p value of SN 1006 will increase up to several 10^{49} erg in the next 5 kyr, even if the

Table 1
Comparison of Physical Properties in 13 Gamma-Ray SNRs

Name	Distance (kpc)	Diameter (pc)	Age (kyr)	n_p (cm^{-3})	W_p (10^{49} erg)	References
(1)	(2)	(3)	(4)	(5)	(6)	(7)
SN 1006	2.2 (a)	18	1.0	25	$0.016^{+0.004}_{-0.004}$	This work
RX J1713.7−3946	1.0	18	1.6	130	$0.10^{+0.05}_{-0.05}$	Fukui et al. (2021)
RX J0852.0−4622	0.75 (b)	24	1.7 (a)	100	$0.07^{+0.02}_{-0.02}$	Fukui et al. (2017)
RCW 86	2.5	30	1.8	75	$0.11^{+0.01}_{-0.01}$	Sano et al. (2019b)
HESS J1731−347	5.7	44	4.0	60	$0.66^{+0.22}_{-0.22}$	Fukuda et al. (2014)
G39.2−0.3	6.2	14	$5.0^{+2.0}_{-2.0}$ (c)	400	$3.2^{+1.1}_{-0.8}$	de Oña Wilhelmi et al. (2020)
W49B	11.0	16	$6.0^{+1.0}_{-1.0}$ (d)	650	$2.1^{+1.1}_{-0.6}$	Sano et al. (2021b)
Kes 79	5.5	16	$8.3^{+0.5}_{-0.5}$	360	0.5	Kuriki et al. (2018)
G346.6−0.2	11.1	21	$14.0^{+2.0}_{-2.0}$	280	<0.09	Sano et al. (2021a)
W44	3.0 (e)	27	20.0 (f)	200	1.0	Yoshiike et al. (2013)
IC 443	1.5 (g)	20	$25.0^{+5.0}_{-5.0}$ (h)	680	0.09	Yoshiike et al. (2022)
LMC N132D	50.0	25	$2.5^{+0.2}_{-0.2}$ (j)	<2000	>0.5	Sano et al. (2020)
LMC N63A	50.0	18	$3.5^{+1.5}_{-1.5}$ (j)	190	$0.9^{+0.5}_{-0.6}$	Sano et al. (2019a)

Note. Column (1): name of SNRs. Column (2): distance to SNRs in units of kiloparsec. Column (3): diameter of SNRs in units of parsec. Column (4): age of SNRs in units of kiloyears. Column (5): averaged number density of total interstellar protons n_p in units of centimeter^{-3}. Column (6): total energy of cosmic-ray protons W_p in units of 10^{49} erg. Column (7): references for CO/H I-derived n_p and W_p for each SNR. Other specific references are also shown as follows: (a) Winkler et al. (2003), (b) Katsuda et al. (2008), (c) Su et al. (2011), (d) Zhou & Vink (2018), (e) Caswell et al. (1975), (f) Wolszczan et al. (1991), (g) Welsh & Sallmen (2003), (h) Olbert et al. (2001), Lee et al. (2008), (i) Law et al. (2020), (j) Hughes et al. (1998).

forward shock has already reached the wind shell (see also Section 4.1). Since it is unlikely that the decelerated forward shock would continue to accelerate cosmic rays for the next 5 kyr, some other mechanisms to increasing W_p are needed.

One possible idea is that the cosmic-ray diffusion into the wind wall also plays an important role in understanding the values of W_p in the early evolutional stage of the SNRs. In this scenario, cosmic rays are mainly accelerated inside the low-density wind bubble via the DSA scheme. After the shock has reached the wind wall, cosmic rays diffuse into the wind wall. The penetration depth of cosmic-ray protons l_{pd} can be derived by (Inoue et al. 2012):

$$l_{pd} = 0.1\ \eta^{0.5}(E/10\ \mathrm{TeV})^{0.5}(B/100\ \mu\mathrm{G})^{-0.5} \times (t/1000\ \mathrm{yr})^{0.5}\ \mathrm{pc}, \quad (3)$$

where η is gyro-factor (>1), E is the energy of cosmic rays, B is the magnetic field, and t is the age of the SNR. By adopting $\eta = 4$ for the inert-cloud region (Tanaka et al. 2020), $E = 100$ TeV, and $B = 45$ μG (Acero et al. 2010), the penetration depth of cosmic-ray protons l_{pd} is to be ∼0.9 pc for $t = 1$ kyr and ∼2.3 pc for $t = 6$ kyr. Because the thickness of the wind shell is to be ∼1.9 pc, accelerated cosmic-ray protons will be fully interacting with the H I clouds within the wind shell in the next 5 kyr. In short, accelerated cosmic rays below 100 TeV are trapped within the wind cavity if the SNR age is young enough.

It should be also noted that the derived W_p values except for RX J1713.7−3946 likely have additional uncertainties (by a factor of two or three) due to the difficulty in separation of the hadronic and leptonic gamma-rays by the SED modeling alone (e.g., Inoue et al. 2012). According to Fukui et al. (2021), each gamma-ray component can be accurately distinguished by a comparison of gamma-ray, synchrotron X-ray, and total interstellar proton images. They found that hadronic gamma-ray contribution for RX J1713.7−3946 is (67 ± 8)% of the total gamma-rays, and hence the accuracy of W_p (and the hadronic gamma-ray luminosity) in RX J1713.7−3946 is significantly better than that in other SNRs derived using the SED modeling results. Moreover, all derived W_p values should be considered as an upper limit because we assume the uniform density distribution of the ISM protons within the shell. Nevertheless, we can find the global trend between the age and W_p by three orders of magnitude, implying that the trend itself is reliable.

In any case, the young (age < 6 kyr) gamma-ray SNRs including SN 1006 show a good correlation between the SNR age and W_p, possibly suggesting that the diffusion timescale is important in understanding in situ values of W_p. Further gamma-ray and H I observations at the high-angular resolution using the Cherenkov Telescope Array (Actis et al. 2011; Cherenkov Telescope Array Consortium et al. 2019) and the Australian Square Kilometre Array Pathfinder (ASKAP; Johnston et al. 2007; Hotan et al. 2021) will allow us to reveal the diffusion mechanisms of cosmic rays in detail.

5. Conclusions

We summarize our conclusions as follows:

1. New H I observations using the ATCA have revealed the spatial and kinematic distributions of H I clouds associated with the Type Ia supernova remnant SN 1006. The H I clouds at $V_{LSR} = 4.0$–12.0 km s^{-1} show a good spatial correspondence with the X-ray shell, particularly in the southwest, northwest, and northeast. The total mass of H I clouds is ∼1000 $M_\odot$ and the averaged atomic hydrogen column density is ∼4×10^{20} cm^{-2} by assuming the optically thick H I.
2. The H I cavity-like distributions in the position–velocity and radius–velocity diagrams indicate the expanding shell, whose expansion velocity is ∼4 km s^{-1} with the systemic velocity of 8 ± 2 km s^{-1}. By considering the pre- and postshocked gas density and spatial extent of the expanding shell, the expanding H I shell was likely formed by strong winds from the progenitor system, and

then the forward shock of SN 1006 has already reached its wind wall. This scenario coexists with the conventional distance of 2.2 kpc because SN 1006 and its surroundings do not follow the Galactic rotation owing to their large distances from the Galactic plane.

3. We proposed a possible scenario that the progenitor system of SN 1006 consists of a white dwarf and a companion star, namely the single-degenerate system because the kinematics of the H I expanding shell can be explained by accretion winds from the progenitors.
4. The total energy of accelerated cosmic-ray protons W_p is derived to be only ~ 1.2–2.0×10^{47} erg by adopting the averaged interstellar proton density of $\sim 25\,\mathrm{cm}^{-3}$. This small value is compatible with a positive correlation between the age and W_p of other gamma-ray supernova remnants with an age less than $\sim$6 kyr. Since the forward shock of SN 1006 has already reached the wind shell and was decelerated, a time-dependent evolution of W_p is possibly relating the cosmic-ray diffusion into the H I wind shell. The cosmic-ray diffusion can increase the W_p value in SN 1006 up to several 10^{49} erg in the next $\sim$5 kyr.

The authors acknowledge Tatsuya Fukuda and Satoshi Yoshiike for contributions on the data reduction and observations of H I. We are also grateful to the anonymous referee for useful comments that helped us improve the paper significantly. The Australia Telescope Compact Array (ATCA) and the Parkes radio telescope are parts of the Australia Telescope National Facility, which is funded by the Australian Government for operation as a National Facility managed by CSIRO. We acknowledge the Gomeroi people as the traditional owners of the Observatory site. The scientific results reported in this article are based on data obtained from the Chandra Data Archive (Obs IDs: 3838, 4385–4394, 13738–13743, 14423, 14424, 14435). This research has made use of the software provided by the Chandra X-ray Center in the application packages CIAO (v 4.12). This work was supported by JSPS KAKENHI grant Nos. JP19H05075[10] (H.S.), JP20KK0309[11] (H. S.), and JP21H01136[12] (H. S.).

Facilities: ATCA, Parkes, Chandra (CXO), H.E.S.S., Fermi.

Software: IDL Astronomy User's Library (Landsman 1993), MIRIAD (Sault et al. 1995), CIAO (v 4.12; Fruscione et al. 2006), CALDB (v 4.9.1; Graessle et al. 2007), KARMA (Gooch 1996).

ORCID iDs

H. Sano https://orcid.org/0000-0003-2062-5692
H. Yamaguchi https://orcid.org/0000-0002-5092-6085
M. Aruga https://orcid.org/0000-0001-5069-5988
Y. Fukui https://orcid.org/0000-0002-8966-9856
K. Tachihara https://orcid.org/0000-0002-1411-5410
M. D. Filipović https://orcid.org/0000-0002-4990-9288
G. Rowell https://orcid.org/0000-0002-9516-1581

References

Acero, F., Aharonian, F., Akhperjanian, A. G., et al. 2010, A&A, 516, A62
Acero, F., Ballet, J., & Decourchelle, A. 2007, A&A, 475, 883
Actis, M., Agnetta, G., Aharonian, F., et al. 2011, ExA, 32, 193
Aharonian, F. A., & Atoyan, A. M. 1996, A&A, 309, 917
Alsaberi, R. Z. E., Barnes, L. A., Filipović, M. D., et al. 2019, Ap&SS, 364, 204
Badenes, C., Hughes, J. P., Bravo, E., et al. 2007, ApJ, 662, 472
Bamba, A., Fukazawa, Y., Hiraga, J. S., et al. 2008, PASJ, 60, S153
Bamba, A., Yamazaki, R., Ueno, M., et al. 2003, ApJ, 589, 827
Bedin, L. R., Ruiz-Lapuente, P., González Hernández, J. I., et al. 2014, MNRAS, 439, 354
Bell, A. R. 1978, MNRAS, 182, 147
Blandford, R. D., & Ostriker, J. P. 1978, ApJL, 221, L29
Bozzetto, L. M., Filipović, M. D., Vukotić, B., et al. 2017, ApJS, 230, 2
Brand, J., & Blitz, L. 1993, A&A, 275, 67
Cassam-Chenaï, G. ., Hughes, J. P., Reynoso, E. M., et al. 2008, ApJ, 680, 1180
Caswell, J. L., Murray, J. D., Roger, R. S., et al. 1975, A&A, 45, 239
Cherenkov Telescope Array Consortium, Acharya, B. S., Agudo, I, et al. 2019, Science with the Cherenkov Telescope Array (Singapore: World Scientific)
Condon, B., Lemoine-Goumard, M., Acero, F., et al. 2017, ApJ, 851, 100
de Oña Wilhelmi, E., Sushch, I., Brose, R., et al. 2020, MNRAS, 497, 3581
Dubner, G. M., Giacani, E. B., Goss, W. M., et al. 2002, A&A, 387, 1047
Filipović, M. D., Payne, J. L., Alsaberi, R. Z. E., et al. 2022, MNRAS, 512, 265
Fruscione, A., McDowell, J. C., Allen, G. E., et al. 2006, Proc. SPIE, 6270, 62701V
Fukuda, T., Yoshiike, S., Sano, H., et al. 2014, ApJ, 788, 94
Fukui, Y., Hayakawa, T., Inoue, T., et al. 2018, ApJ, 860, 33
Fukui, Y., Moriguchi, Y., Tamura, K., et al. 2003, PASJ, 55, L61
Fukui, Y., Okamoto, R., Kaji, R., et al. 2014, ApJ, 796, 59
Fukui, Y., Sano, H., Sato, J., et al. 2012, ApJ, 746, 82
Fukui, Y., Sano, H., Sato, J., et al. 2017, ApJ, 850, 71
Fukui, Y., Sano, H., Yamane, Y., et al. 2021, ApJ, 915, 84
Fukui, Y., Torii, K., Onishi, T., et al. 2015, ApJ, 798, 6
Fukushima, K., Yamaguchi, H., Slane, P. O., et al. 2020, ApJ, 897, 62
Gabici, S. 2013, Cosmic Rays in Star-forming Environments (Berlin: Springer), 221
González Hernández, J. I., Ruiz-Lapuente, P., Filippenko, A. V., et al. 2009, ApJ, 691, 1
González Hernández, J. I., Ruiz-Lapuente, P., Tabernero, H. M., et al. 2012, Natur, 489, 533
Gooch, R. 1996, in ASP Conf. Ser., 101, Karma: A Visualization Test-bed, ed. G. H. Jacoby & J. Barnes (San Francisco, CA: ASP), 80
Graessle, D. E., Evans, I. N., Glotfelty, K., et al. 2007, Chandra Newsletter, 14, 33
Hachisu, I., & Kato, M. 2003a, ApJ, 590, 445
Hachisu, I., & Kato, M. 2003b, ApJ, 598, 527
Hachisu, I., Kato, M., & Nomoto, K. 1996, ApJL, 470, L97
Hachisu, I., Kato, M., & Nomoto, K. 1999a, ApJ, 522, 487
Hachisu, I., Kato, M., Nomoto, K., et al. 1999b, ApJ, 519, 314
Hachisu, I., Kato, M., & Nomoto, K. 2008, ApJ, 679, 1390
Hayashi, K., Mizuno, T., Fukui, Y., et al. 2019, ApJ, 884, 130
Hotan, A. W., Bunton, J. D., Chippendale, A. P., et al. 2021, PASA, 38, e009
Hughes, J. P., Hayashi, I., & Koyama, K. 1998, ApJ, 505, 732
Iben, I., & Tutukov, A. V. 1984, ApJS, 54, 335
Inoue, T., Yamazaki, R., Inutsuka, S.-i., et al. 2012, ApJ, 744, 71
Ivanova, N., Justham, S., Chen, X., et al. 2013, A&ARv, 21, 59
Johnston, S., Bailes, M., Bartel, N., et al. 2007, PASA, 24, 174
Kalberla, P. M. W., McClure-Griffiths, N. M., Pisano, D. J., et al. 2010, A&A, 521, A17
Katsuda, S., Petre, R., Long, K. S., et al. 2009, ApJL, 692, L105
Katsuda, S., Tsunemi, H., & Mori, K. 2008, ApJL, 678, L35
Kerr, F. J., & Lynden-Bell, D. 1986, MNRAS, 221, 1023
Kerzendorf, W. E., Long, K. S., Winkler, P. F., et al. 2018a, MNRAS, 479, 5696
Kerzendorf, W. E., Schmidt, B. P., Laird, J. B., et al. 2012, ApJ, 759, 7
Kerzendorf, W. E., Strampelli, G., Shen, K. J., et al. 2018b, MNRAS, 479, 192
Kerzendorf, W. E., Yong, D., Schmidt, B. P., et al. 2013, ApJ, 774, 99
Kirshner, R., Winkler, P. F., & Chevalier, R. A. 1987, ApJL, 315, L135
Koo, B.-C., & Heiles, C. 1991, ApJ, 382, 204
Koo, B.-C., Reach, W. T., Heiles, C., et al. 1990, ApJ, 364, 178
Koyama, K., Petre, R., Gotthelf, E. V., et al. 1995, Natur, 378, 255
Kuriki, M., Sano, H., Kuno, N., et al. 2018, ApJ, 864, 161
Landsman, W. B. 1993, in Astronomical Data Analysis Software and Systems II, ASP Conf. Ser. 52 (San Francisco, CA: ASP), 246
Law, C. J., Milisavljevic, D., Patnaude, D. J., et al. 2020, ApJ, 894, 73
Lee, J.-J., Koo, B.-C., Yun, M. S., et al. 2008, AJ, 135, 796
Li, J.-T., Ballet, J., Miceli, M., et al. 2018, ApJ, 864, 85

[10] https://kaken.nii.ac.jp/en/grant/KAKENHI-PUBLICLY-19H05075/
[11] https://kaken.nii.ac.jp/en/grant/KAKENHI-PROJECT-20KK0309/
[12] https://kaken.nii.ac.jp/en/grant/KAKENHI-PROJECT-21H01136/

Li, J.-T., Decourchelle, A., Miceli, M., et al. 2015, MNRAS, 453, 3953
Long, K. S., Reynolds, S. P., Raymond, J. C., et al. 2003, ApJ, 586, 1162
Lopez, L. A., Ramirez-Ruiz, E., Badenes, C., et al. 2009, ApJL, 706, L106
Maeda, K., & Terada, Y. 2016, IJMPD, 25, 1630024
Maoz, D., Mannucci, F., & Nelemans, G. 2014, ARA&A, 52, 107
Maxted, N. I., Filipović, M. D., Sano, H., et al. 2018, ApJ, 866, 76
McClure-Griffiths, N. M., Pisano, D. J., Calabretta, M. R., et al. 2009, ApJS, 181, 398
Miceli, M., Acero, F., Dubner, G., et al. 2014, ApJL, 782, L33
Miceli, M., Bocchino, F., Decourchelle, A., et al. 2012, A&A, 546, A66
Nomoto, K. 1982, ApJ, 257, 780
Nomoto, K., Suzuki, T., Deng, J., et al. 2005, in ASP Conf. Ser. 342, 1604-2005: Supernovae as Cosmological Lighthouses, ed. M. Turatto et al. (San Francisco, CA: ASP), 105
Ohira, Y., Murase, K., & Yamazaki, R. 2010, A&A, 513, A17
Okamoto, R., Yamamoto, H., Tachihara, K., et al. 2017, ApJ, 838, 132
Olbert, C. M., Clearfield, C. R., Williams, N. E., et al. 2001, ApJL, 554, L205
Paczynski, B. 1985, in Cataclysmic Variables and Low-Mass X-ray Binaries, ed. D. Q. Lamb & J. Patterson (Dordrecht: Reidel), 1
Perlmutter, S., Aldering, G., Goldhaber, G., et al. 1999, ApJ, 517, 565
Planck Collaboration, Abergel, A., Ade, P. A. R., et al. 2014, A&A, 571, A11
Raymond, J. C., Korreck, K. E., Sedlacek, Q. C., et al. 2007, ApJ, 659, 1257
Ruiz-Lapuente, P. 2019, NewAR, 85, 101523
Ruiz-Lapuente, P., González Hernández, J. I., Mor, R., et al. 2019, ApJ, 870, 135
Sano, H., Fukuda, T., Yoshiike, S., et al. 2015, ApJ, 799, 175
Sano, H., Matsumura, H., Nagaya, T., et al. 2019a, ApJ, 873, 40
Sano, H., Plucinsky, P. P., Bamba, A., et al. 2020, ApJ, 902, 53
Sano, H., Reynoso, E. M., Mitsuishi, I., et al. 2017, JHEAp, 15, 1
Sano, H., Rowell, G., Reynoso, E. M., et al. 2019b, ApJ, 876, 37
Sano, H., Sato, J., Horachi, H., et al. 2010, ApJ, 724, 59
Sano, H., Suzuki, H., Nobukawa, K. K., et al. 2021a, ApJ, 923, 15
Sano, H., Tanaka, T., Torii, K., et al. 2013, ApJ, 778, 59
Sano, H., Yamane, Y., Tokuda, K., et al. 2018, ApJ, 867, 7
Sano, H., Yoshiike, S., Yamane, Y., et al. 2021b, ApJ, 919, 123
Sault, R. J., Teuben, P. J., & Wright, M. C. H. 1995, in Astronomical Data Analysis Software and Systems IV, ASP Conf. Ser. 77 (San Francisco, CA: ASP), 433
Schaefer, B. E. 1996, ApJ, 459, 438
Schweizer, F., & Middleditch, J. 1980, ApJ, 241, 1039
Seifried, D., Beuther, H., Walch, S., et al. 2022, MNRAS, 512, 4765
Stephenson, F. R., & Green, D. A. (ed.) 2002, Historical Supernovae and their Remnants (Oxford: Clarendon), 5
Su, Y., Chen, Y., Yang, J., et al. 2011, ApJ, 727, 43
Tanaka, T., Okuno, T., Uchida, H., et al. 2021, ApJL, 906, L3
Tanaka, T., Uchida, H., Sano, H., et al. 2020, ApJL, 900, L5
Uchida, H., Yamaguchi, H., & Koyama, K. 2013, ApJ, 771, 56
Wang, Y., Beuther, H., Rugel, M. R., et al. 2020, A&A, 634, A83
Weaver, R., McCray, R., Castor, J., et al. 1977, ApJ, 218, 377
Webbink, R. F. 1984, ApJ, 277, 355
Welsh, B. Y., & Sallmen, S. 2003, A&A, 408, 545
Whelan, J., & Iben, I. 1973, ApJ, 186, 1007
Winkler, P. F., Gupta, G., & Long, K. S. 2003, ApJ, 585, 324
Winkler, P. F., Williams, B. J., Blair, W. P., et al. 2013, ApJ, 764, 156
Winkler, P. F., Williams, B. J., Reynolds, S. P., et al. 2014, ApJ, 781, 65
Wolszczan, A., Cordes, J. M., & Dewey, R. J. 1991, ApJL, 372, L99
Woods, T. E., Ghavamian, P., Badenes, C., et al. 2017, NatAs, 1, 800
Xing, Y., Wang, Z., Zhang, X., et al. 2016, ApJ, 823, 44
Xing, Y., Wang, Z., Zhang, X., et al. 2019, PASJ, 71, 77
Xue, Z., & Schaefer, B. E. 2015, ApJ, 809, 183
Yamaguchi, H., Badenes, C., Petre, R., et al. 2014, ApJL, 785, L27
Yamaguchi, H., Koyama, K., Katsuda, S., et al. 2008, PASJ, 60, S141
Yoshiike, S., Fukuda, T., Sano, H., et al. 2013, ApJ, 768, 179
Yoshiike, S., Sano, H., Fukuda, T., et al. 2022, submitted
Zhou, P., Chen, Y., Zhang, Z.-Y., et al. 2016, ApJ, 826, 34
Zhou, P., & Vink, J. 2018, A&A, 615, A150